First-Principles Investigation of CO Adsorption on h-Fe₇C₃ Catalyst

Jinzhe Fu [1], Deshuai Sun [1],*, Zhaojun Chen [1], Jian Zhang [2] and Hui Du [1],*

[1] College of Chemistry and Chemical Engineering, Qingdao University, Qingdao 266071, China; 2017020822@qdu.edu.cn (J.F.); qdhxhgxy@163.com (Z.C.)

[2] Soda ash plant of Shandong Haihua Co., Ltd., Weifang 262737, China; zjaccess@126.com

* Correspondence: luckysds@qdu.edu.cn (D.S.); duhui@qdu.edu.cn (H.D.)

check for updates

Abstract: h-Fe₇C₃ is considered as the main active phase of medium-temperature Fe-based Fischer–Tropsch catalysts. Basic theoretical guidance for the design and preparation of Fe-based Fischer–Tropsch catalysts can be obtained by studying the adsorption and activation behavior of CO on h-Fe₇C₃. In this paper, the first-principles method based on density functional theory is used to study the crystal structure properties of h-Fe₇C₃ and the adsorption and activation CO on its low Miller index surfaces $(1\bar{1}0), (1\bar{1}1), (101), (1\bar{1}\bar{1})$ and (001). It was found that the low Miller index crystal plane of h-Fe₇C₃ crystal has multiple equivalent crystal planes and that the maximum adsorption energy of CO at the 3F2 point of the $(1\bar{1}1)$ plane is −2.50 eV, indicating that h-Fe₇C₃ has a better CO adsorption performance. In addition, the defects generated at the truncated position of the h-Fe₇C₃ crystal plane have a great impact on the adsorption energy of CO on its surface, that is, the adsorption energy of CO on Fe atoms with C vacancies is higher. The activity of CO after adsorption is greatly affected by the adsorption configuration and less affected by the adsorption energy. The higher the coordination number of Fe atoms after adsorption, the higher the CO activity. At the same time, it was found that the bonding of O and Fe atoms is conducive to the activation of CO.

Keywords: Fischer–Tropsch synthesis; h-Fe₇C₃; quantum chemistry; adsorption activation

1. Introduction

Due to the increasing demand for petroleum in human industrial production and life, the conversion of synthesis gas (CO + H₂) into fuel and high-value organic chemicals through Fischer–Tropsch synthesis has been receiving increasing attention [1–3]. Owing to their high activity, high selectivity and low cost and the flexible distribution of low H₂/CO synthesis gas conversion products, iron-based catalysts are widely used in the Fischer–Tropsch synthesis industry [4]. However, the phase types of Fe-based catalysts during Fischer–Tropsch synthesis are very complicated, and the understanding of their catalytic mechanism is not clear. Therefore, the active phase structure type and catalytic mechanism of iron-based catalysts need to be further studied to provide theoretical guidance for the design and preparation of new and efficient Fischer–Tropsch synthesis catalysts.

When an iron-based catalyst is used in the Fischer–Tropsch synthesis reaction, the catalyst precursor (α-Fe₂O₃) is first reduced to magnetite (Fe₃O₄) [5,6] and then converted into a mixture of iron oxide and carbide phases during the reaction, such as ε-Fe₂C, έ-Fe₂.₂C, χ-Fe₅C₂, θ-Fe₃C and h-Fe₇C₃ [7,8]. Among them, Hägg carbide (χ-Fe₅C₂) and Fe₂C are considered as the main active phases [9]. However, in recent research, the catalytic activity of h-Fe₇C₃ in medium-temperature Fischer–Tropsch synthesis (260–300 °C) was found to be higher than that of χ-Fe₅C₂ and ε-Fe₂C by Li Yongwang's team [10]. At present, the research on the catalytic mechanism in the medium-temperature

Fischer–Tropsch synthesis reaction needs to be deepened, and the adsorption activation behavior of CO on the h-Fe_7C_3 surface has not been reported. In this paper, the characteristics of the crystal structure of h-Fe_7C_3, as well as the adsorption and activation of CO on its low Miller index crystal planes, were studied through the first-principles method of density functional theory to provide basic theoretical guidance for designing, preparing and controlling Fischer–Tropsch synthesis catalysts.

2. Calculation Methods

All calculations in this paper were conducted with the CASTEP(Cambridge Sequential Total Energy Package) according to the density functional theory (DFT). The Perdew–Burke–Ernzerh (PBE) functional in the generalized gradient approximation (GGA) was employed in the electron exchange correlation potential [11–13]. Spin polarization was included for all calculations on the ferromagnetic h-Fe_7C_3 system to deal with an accurate description of magnetic properties by fixing the initial number of spins of each iron atom to 4. In order to calculate the plane wave basis set, the cut-off energy, the convergence accuracy of the self-consistent field and the k point were set as 400 eV, 2×10^{-6} eV/atom and $3 \times 3 \times 1$, respectively. Meanwhile, all atoms were allowed to be fully relaxed for calculating the h-Fe_7C_3 unit cell structure. Furthermore, 28 iron atoms and 12 carbon atoms were used as crystal planes with the fixation of underlying atoms in order to reduce the calculation quantity while the adsorption of crystal planes and CO on the h-Fe_7C_3 crystal plane was calculated. Moreover, a vacuum layer of 15 Å was added to the crystal planes to prevent applied forces between crystal planes from interfering calculation results.

We utilized h-Fe_7C_3 as the unit cell structure, in accordance with a literature report, with the space group of $P6_3mc$. Fourteen iron atoms and six carbon atoms were contained in the crystal lattice [10,14]. There were a total of 12 symmetric elements in the $P6_3mc$ symmetric group, including one threefold rotor, three screw axes, three mirror planes and three glide planes, as well as identity operations. Identical crystal planes were searched in line with the symmetry of h-Fe_7C_3, so as to avoid repeated selection of crystal planes. The basic idea is presented as follows: First, a coordinate system is established with three crystal axes; then, the direction vector $\vec{\beta}$ of the crystal plane is obtained through two vectors, $\vec{\alpha_1}$ and $\vec{\alpha_2}$, on the crystal plane (hkl). On this basis, $\vec{\beta}$ and A on the plane are symmetrically operated so that they can be symmetric with the direction vector $\vec{\gamma}$ on the crystal plane and B on the plane. Ultimately, $\vec{\gamma}$ and the point B are employed to solve the equation of the symmetric crystal plane, thus obtaining the intercept and Miller index. Specifically:

1. $\vec{\alpha_1} = \left(\frac{1}{h}, -\frac{1}{k}, 0\right)$ and $\vec{\alpha_2} = \left(0, \frac{1}{k}, -\frac{1}{l}\right)$, two vectors on the crystal plane, are obtained according to the Miller index of the crystal plane. Since it is difficult to obtain the vector product from a coordinate system that is not an orthogonal coordinate system ($\alpha = \beta = 90°, \gamma = 120°$), the vector product $\vec{\beta'}$ is solved by transforming the coordinates into the coordinates $\vec{\alpha'}$ in the orthogonal coordinate system, and then the vector product is obtained before $\vec{\beta'}$ is converted into $\vec{\beta}$, as shown in Equation (1), Equation (2) and Equation (3):

$$\vec{\alpha}C = \vec{\alpha'} \tag{1}$$

$$\vec{\beta'} = \vec{\alpha'}_1 \times \vec{\alpha'}_2 \tag{2}$$

$$\vec{\beta'}C^{-1} = \vec{\beta} \tag{3}$$

where $C = \begin{bmatrix} 1 & 0 & 0 \\ \frac{-1}{2} & \frac{\sqrt{3}}{2} & 0 \\ 0 & 0 & 1 \end{bmatrix}$ and $C^{-1} = \begin{bmatrix} 1 & 0 & 0 \\ \frac{\sqrt{3}}{3} & \frac{2\sqrt{3}}{3} & 0 \\ 0 & 0 & 1 \end{bmatrix}$.

2. $\vec{\gamma} = (a, b, c)$ and the point $B(x_2, y_2, z_2)$ are obtained by conducting symmetric operation on $\vec{\beta}$ and the point $A(x_1, y_1, z_1)$ on the crystal plane based on the general equivalent point system of the P6$_3$mc symmetry group (see Table 1).

3. The intercept of the crystal plane on the coordinate axis is solved by the plane equation in the current coordinate system, as shown in Equations (4) and (5):

$$\vec{\gamma}C\left(\begin{bmatrix} x - x_2 & y - y_2 & z - z_2 \end{bmatrix}C\right)^T = 0 \tag{4}$$

$$\left(a - \frac{1}{2}b\right)(x - x_2) + \left(-\frac{1}{2}a + b\right)(y - y_2) + c(z - z_2) = 0 \tag{5}$$

where C is the transformation matrix of the above-mentioned coordinate.

4. The Miller index of the symmetric crystal plane can be obtained from calculating the intercept with the plane equation. Besides, the stability of the crystal plane is measured by the surface energy, as shown in Equation (6):

$$E_{surface} = \frac{(E_n - n \times E_{bulk})}{2 \times A} \tag{6}$$

where E_n is the total energy of the n-layer crystal plane, E_{bulk} is the energy of a single-layer unit cell, n is the number of layers of unit cell and A is the area of the crystal plane. The smaller the surface energy, the more stable the crystal plane will be [15]. The adsorption of CO on h-Fe$_7$C$_3$ is expressed by its adsorption energy:

$$E_{ads} = E_{CO/slab} - E_{slab} - E_{CO} \tag{7}$$

where $E_{CO/slab}$ represents the energy adsorbed by CO on the crystal plane, E_{slab} is the energy of the crystal plane and E_{CO} is the energy of free CO. The more negative the adsorption energy, the more stable the adsorption of CO on the crystal plane will be.

Table 1. Surface energy results for the h-Fe$_7$C$_3$ surfaces.

Surface	Surface Energy (J/m^2)	Surface	Surface Energy (J/m^2)
$(1\bar{1}0)$	2.55	$(3\bar{3}0)$	2.91
$(1\bar{1}1)$	2.58	$(4\bar{4}0)$	2.96
(101)	2.64	$(4\bar{4}\bar{4})$	3.09
$(1\bar{1}\bar{1})$	2.78	$(\bar{4}0\bar{4})$	3.29
(001)	2.84	$(4\bar{4}\bar{4})$	3.30

3. Results and Discussion

3.1. Calculation Results of the h-Fe$_7$C$_3$ Crystal Plane

The result of the optimized h-Fe$_7$C$_3$ structure is shown in Figure 1. Unit cell parameters are a = b = 6.788 Å, c = 4.445 Å, $\alpha = \beta = 90°$ and $\gamma = 120°$, approaching the experimental values (a = b = 6.88 Å, c = 4.54 Å, $\alpha = \beta = 90°$ and $\gamma = 120°$) [16].
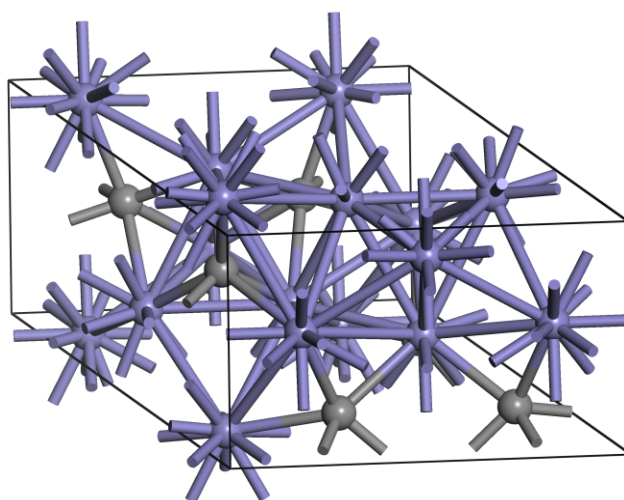
4 of 10

Figure 1. h-Fe_7C_3 structure (Fe is in blue and C is in gray).

The surface energy calculation results for 10 crystal planes are shown in Table 1.

As can be seen from Table 1, the surface energy of a surface with a low Miller index is significantly lower than that of a surface with a high Miller index; furthermore, the $(1\bar{1}0)$ plane is the most stable among the surfaces with low Miller indexes. The crystal plane with low surface energy is more stable in thermodynamics, with a higher probability of occurring during crystal formation. In that case, five crystal surfaces with lower surface energy were selected for calculating CO adsorption and activation.

To avoid repeated selection of crystal planes, symmetric crystal planes of $(1\bar{1}0)$, $(1\bar{1}1)$, (101), $(1\bar{1}\bar{1})$ and (001) were calculated, as shown in Table 2.

Table 2. Symmetric crystal planes of some crystal planes of h-Fe_7C_3.

General Equivalent Point System	$(1\bar{1}0)$	$(1\bar{1}1)$	(101)	$(1\bar{1}\bar{1})$	(001)
x, y, z	$(1\bar{1}0)$	$(1\bar{1}1)$	(101)	$(1\bar{1}\bar{1})$	(001)
−y, x − y, z	(010)	(011)	$(\bar{1}11)$	$(01\bar{1})$	
−x + y, −x, z	$(\bar{1}00)$	$(\bar{1}01)$	$(0\bar{1}1)$	$(\bar{1}0\bar{1})$	
−x, −y, z + 1/2	$(\bar{1}10)$	$(\bar{2}22)$	$(\bar{2}02)$	$(\bar{2}2\bar{2})$	(002)
y, −x + y, z + 1/2	$(0\bar{1}0)$	$(0\bar{2}2)$	$(2\bar{2}2)$	$(0\bar{2}\bar{2})$	(002)
x − y, x, z + 1/2	(100)	(202)	(022)	$(20\bar{2})$	(002)
−y, −x, z	$(1\bar{1}0)$	$(1\bar{1}1)$	$(0\bar{1}1)$	$(1\bar{1}\bar{1})$	
−x + y, y, z	$(\bar{1}00)$	$(\bar{1}01)$	$(\bar{1}11)$	$(\bar{1}0\bar{1})$	
x, x − y, z	(010)	(011)	(101)	$(01\bar{1})$	
y, x, z + 1/2	$(\bar{1}10)$	$(\bar{2}22)$	(022)	$(\bar{2}2\bar{2})$	(002)
x − y, −y, z + 1/2	(100)	(202)	$(2\bar{2}\bar{2})$	$(20\bar{2})$	(002)
−x, −x + y, z + 1/2	$(0\bar{1}0)$	$(0\bar{2}2)$	$(\bar{2}02)$	$(0\bar{2}\bar{2})$	(002)

As can be observed from Table 2, $(1\bar{1}0), (1\bar{1}1), (101), (1\bar{1}\bar{1})$ and (001) are not equivalent crystal planes due to symmetry. To be specific, four planes of $(1\bar{1}0), (1\bar{1}1), (101)$ and $(1\bar{1}\bar{1})$ have five identical crystal planes. The crystal plane of the (001) plane remains unchanged after rotation and mirroring as it is perpendicular to the rotation axis. Consequently, it is only identical to the (002) plane. Planes $(1\bar{1}0), (1\bar{1}1)$ and $(1\bar{1}\bar{1})$ are perpendicular to the mirror (110), and all three are symmetric about the (110) plane; the (101) plane is perpendicular to the mirror $(2\bar{1}0)$, and (101) is symmetric about the $(2\bar{1}0)$ plane; finally, as the (001) plane is perpendicular to mirrors (110), $(2\bar{1}0)$ and $(1\bar{2}0)$, and the (001) plane is symmetric about (110), $(2\bar{1}0)$ and $(1\bar{2}0)$.

3.2. CO Adsorption and Activation on the h-Fe₇C₃ Crystal Plane

We calculated the adsorption energies of 4 point positions on the $(1\bar{1}0)$ plane, 7 point positions on the $(1\bar{1}1)$ plane, 7 point positions on the (101) plane, 11 point positions on the $(1\bar{1}\bar{1})$ plane and 8 point positions on the (001) plane (as shown in Figure 2). Results are shown in Table 3.
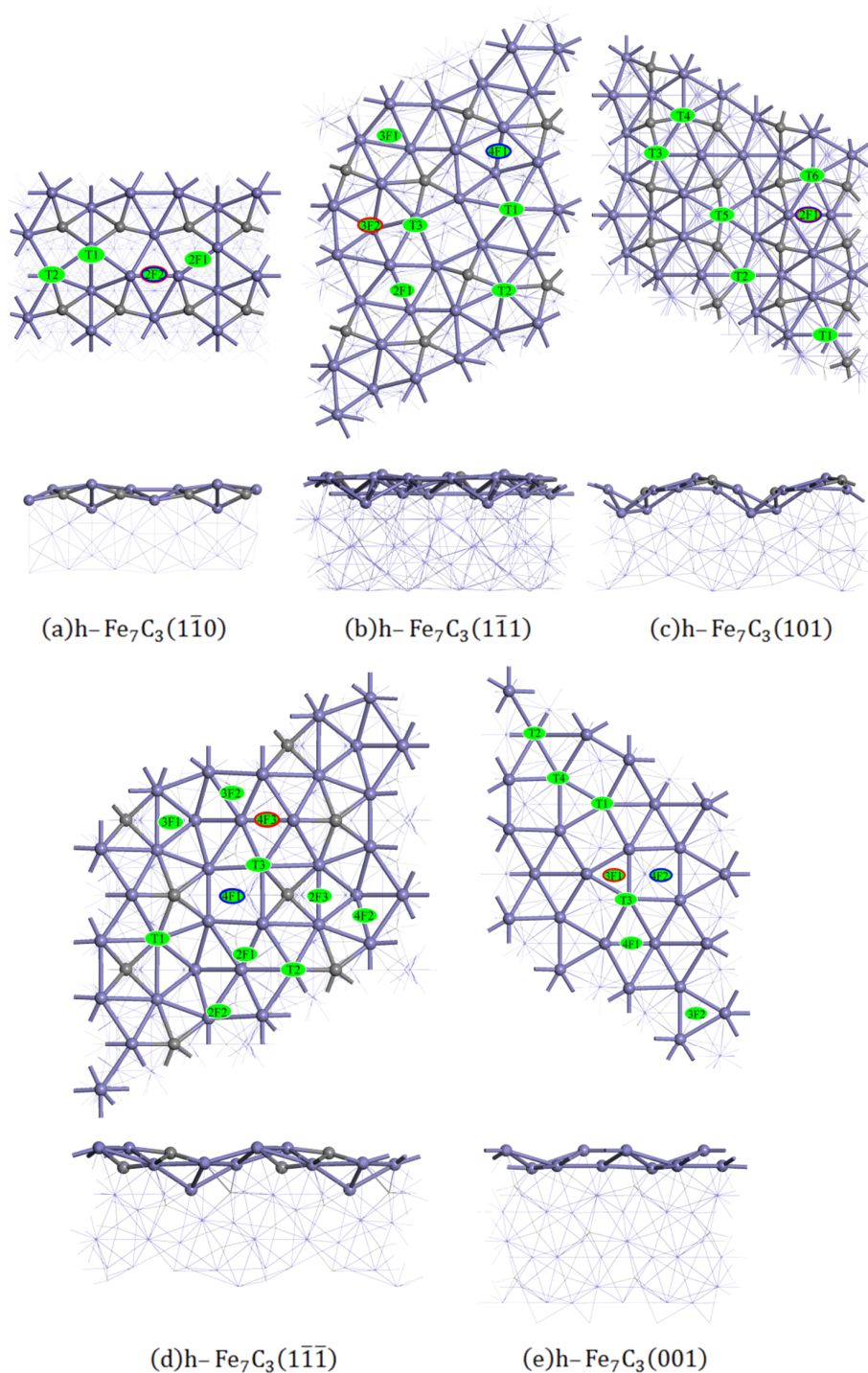

(a)h− Fe₇C₃$(1\bar{1}0)$ (b)h− Fe₇C₃$(1\bar{1}1)$ (c)h− Fe₇C₃(101)

(d)h− Fe₇C₃$(1\bar{1}\bar{1})$ (e)h− Fe₇C₃(001)

Figure 2. CO adsorption on $(1\bar{1}0)$, $(1\bar{1}1)$, (101), $(1\bar{1}\bar{1})$ and (001). C atoms are in gray, and Fe atoms are in blue. T indicates adsorption at the vertex position, and nF indicates n-fold adsorption. The adsorption position with the largest adsorption energy is presented in red box, and the most active point position is presented in blue box (**a**. $(1\bar{1}0)$; **b**. $(1\bar{1}1)$; **c**. (101); **d**. $(1\bar{1}\bar{1})$; **e**. (001)).

Table 3. Absorption energy and bond lengths of five CO adsorption point positions on the h-Fe_7C_3 surface.

Surface	Site	E_{ads}/eV	d(C-O)/Å	d(O-Fe)/Å		d(C-Fe)Å			
$(1\bar{1}0)$	2F1	−2.09	1.191			1.777	2.284		
	2F2	−2.16	1.194			1.883	1.975		
	T1	−2.06	1.180			1.779			
	T2	−2.09	1.182			1.785			
$(1\bar{1}1)$	T1	−1.67	1.177			1.759			
	T2	−1.62	1.175			1.741			
	4F1	−2.45	1.328	2.067	2.275	1.944	2.003	2.006	2.289
	3F1	−1.96	1.221			1.902	2.032	2.042	
	T3	−2.34	1.184			1.762			
	2F1	−1.88	1.201			1.795	2.029		
	3F2	−2.50	1.315	1.996		1.985	1.987	1.990	
(101)	T1	−2.12	1.174			1.771			
	2F1	−2.24	1.196			1.857	1.949		
	T2	−1.01	1.169			1.810			
	T3	−1.73	1.176			1.760			
	T4	−1.63	1.175			1.763			
	T5	−1.29	1.171			1.779			
	T6	−1.60	1.176			1.762			
$(1\bar{1}\bar{1})$	2F1	−2.18	1.200			1.796	2.324		
	T1	−1.78	1.182			1.767			
	2F2	−1.99	1.191			1.784	2.253		
	T2	−1.92	1.179			1.782			
	T3	−2.00	1.179			1.780			
	3F1	−2.08	1.290	2.155		1.943	1.959	1.977	
	3F2	−2.09	1.203			1.839	2.124	2.221	
	4F1	−2.02	1.294	2.156	2.177	1.921	1.930	2.040	2.035
	2F3	−1.70	1.197			1.959	1.982		
	4F2	−1.97	1.274			1.986	1.995	2.006	2.267
	4F3	−2.27	1.220			1.949	1.957	2.269	2.344
(001)	3F1	−2.47	1.202			1.997	1.984	1.989	
	T1	−1.97	1.188			1.763			
	T2	−2.24	1.189			1.750			
	4F1	−2.22	1.219			1.889	2.072	2.251	2.276
	T3	−2.16	1.176			1.790			
	3F2	−1.93	1.211			1.973	1.975	1.981	
	T4	−1.83	1.185			1.772			
	4F2	−2.25	1.310	2.084	2.091	1.927	1.932	2.070	2.072

　　　A weak CO adsorption can be witnessed in the C position, and CO can barely be absorbed on the C position under a low coverage. With only two vertices and two 2F points, few positions on the $(1\bar{1}0)$ plane are suitable for CO absorption, according to Figure 2. The point position with the largest absorbed energy and the most active point position of CO on the $(1\bar{1}0)$ plane are on 2F2 (as shown in Figure 3a), as can be seen from Table 3. The point position with the largest adsorption energy on the $(1\bar{1}1)$ lane is at the 3F2 point position (as shown in Figure 3c), where the adsorption energy can reach up to −2.50 eV; finally, the most active point position is on 4F1, with the CO bond length of 1.328 Å (as shown in Figure 3d). With a plurality of C atoms on the (101) crystal plane, almost all of the CO absorption is at the vertex position with low absorption energy. The point position with the largest absorbed energy and the most active point position of CO on the plane are on 2F1 (as shown in 2F1). The $(1\bar{1}\bar{1})$ crystal plane is similar to that of $(1\bar{1}1)$ without any prominent atoms on the surface, so that there are more positions for CO absorption. The point position with the largest adsorption energy and the most active point position are on 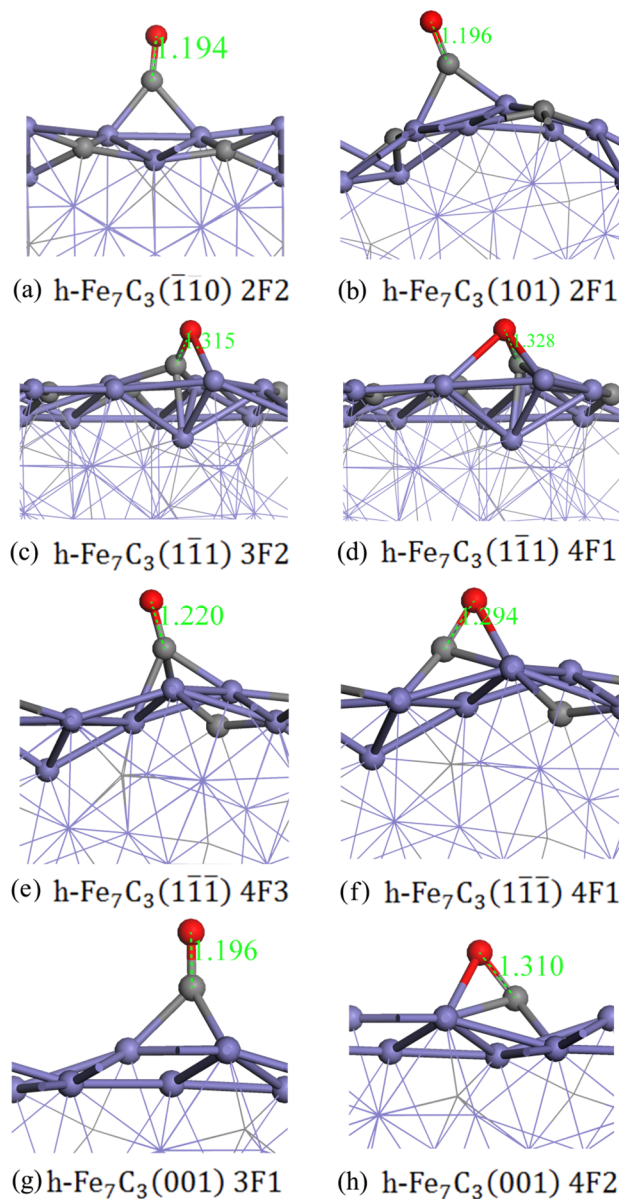4F3 and 4F1, respectively (as shown in Figure 3e,f). Absorbing point positions of the (001) plane with good symmetry are primarily concentrated on

the symmetric axis. The point position with the largest adsorption energy and the most active point position are on 3F1 and 4F2, respectively (as shown in Figure 3g,h).

(a) h-Fe$_7$C$_3$($\bar{1}$10) 2F2

(b) h-Fe$_7$C$_3$(101) 2F1

(c) h-Fe$_7$C$_3$(1$\bar{1}$1) 3F2

(d) h-Fe$_7$C$_3$(1$\bar{1}$1) 4F1

(e) h-Fe$_7$C$_3$(1$\bar{1}\bar{1}$) 4F3

(f) h-Fe$_7$C$_3$(1$\bar{1}\bar{1}$) 4F1

(g) h-Fe$_7$C$_3$(001) 3F1

(h) h-Fe$_7$C$_3$(001) 4F2

Figure 3. The most stable and active adsorption configuration of CO on various crystal planes of h-Fe$_7$C$_3$ (bond length given in Å) (**a**. $\left(1\bar{1}0\right)$2F2; **b**. (101)2F1; **c**. $\left(1\bar{1}1\right)$3F2; **d**. $\left(1\bar{1}1\right)$4F1; **e**. $\left(1\bar{1}\bar{1}\right)$4F3; **f**. $\left(1\bar{1}\bar{1}\right)$4F1; **g**. (001)3F1; **h**. (001)4F2).

It can be seen from Table 3 that the length of the CO bond adsorbing on the h-Fe$_7$C$_3$ will be extended with the increased coordination number of Fe atom coordinates at the point position of adsorption. The longest bond of CO adsorbed at the vertex position is the T2 point (1.189 Å) on the (001) plane; the shortest and the longest bonds are the 2F2 point (1.191 Å) at the 2F position on the $\left(1\bar{1}\bar{1}\right)$ and the 2F1 point (1.201 Å) on the $\left(1\bar{1}1\right)$ plane, respectively; finally, the shortest bond at the 3F position is the 3F1 point (1.202 Å) on the (001) plane. CO activation is significantly affected by the formation of Fe-O bonds. Fe-O bonds are formed at several point positions with the longest CO bonds. Furthermore, CO activation is also affected by the magnitude of the adsorption energy. The adsorption energy at several point positions with short CO bonds exerts a far smaller impact in comparison to the adsorption configuration. For instance, the adsorption energy at the T3 point position on the $\left(1\bar{1}1\right)$ plane is large

(−2.34 eV), while its CO bond length is short (only 1.184 Å). However, the adsorption at the 4F2 point position on the $(1\bar{1}\bar{1})$ is only −1.97 eV, while it has long CO bond, reaching 1.274 Å.

By combining Figure 2 and Table 3, it can be seen that the point positions with large adsorption energy are all around a specific Fe atom, such as 2F2 and T2 on $(1\bar{1}0)$; T3, 3F2 and 4F1 on $(1\bar{1}1)$; T1 and 2F1 on (101); 2F1 and 4F3 on $(1\bar{1}\bar{1})$; and 3F1 on (001). The adsorption energies at these point positions are remarkably higher than other point positions on the same plane. This is because these Fe atoms are in the C-deficient position on the crystal plane, which makes it easier for them to adsorb CO.

The orbital of CO adsorbed on the surfaces is studied by calculating the local density of states (LDOS) of the adsorbed CO molecules. Based on Figure 4, the LDOS was analyzed for CO molecules adsorbed on the five surfaces of h-Fe$_7$C$_3$ with the highest adsorption energy. According to the curves shown in the figure, CO on the $(1\bar{1}0)$2F2 and (101)2F1 has the localized 2π* orbital, which means that the back-donation from the surface to the adsorbed CO molecule is relatively tiny. For the CO on the $(1\bar{1}1)$3F2, the 2π* orbitals are remarkably delocalized, which indicates the increasing back-donation from the surface to antibonding 2π* orbitals. Although the adsorption energy of CO on (001)3F1 and $(1\bar{1}\bar{1})$4F3 is large, the delocalization of the 2π* orbit is not obvious. Based on Figure 5, the d orbital of the Fe atom corresponding with the CO orbital at $(1\bar{1}1)$3F2 has a split nearby E$_f$, while this is not observed on the Fe atom at $(1\bar{1}\bar{1})$4F3 and (001)3F1, indicating that back-donation from the Fe atom to the adsorbed CO molecule is relatively tiny at $(1\bar{1}\bar{1})$4F3 and (001)3F1. This shows that the electron transfer is affected to some extent by the adsorption configuration.
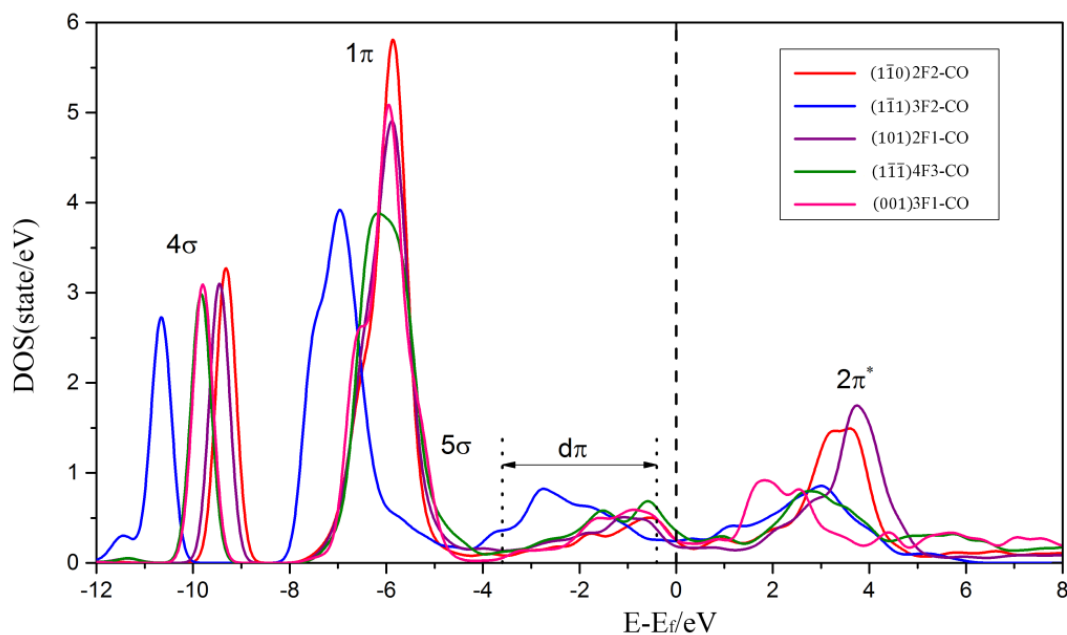

Figure 4. Local density of states (LDOS) of CO adsorbed on the $(1\bar{1}0)$2F2, $(1\bar{1}1)$3F2, (101)2F1, $(1\bar{1}\bar{1})$4F3 and (001)3F1 of the h-Fe$_7$C$_3$ plane.
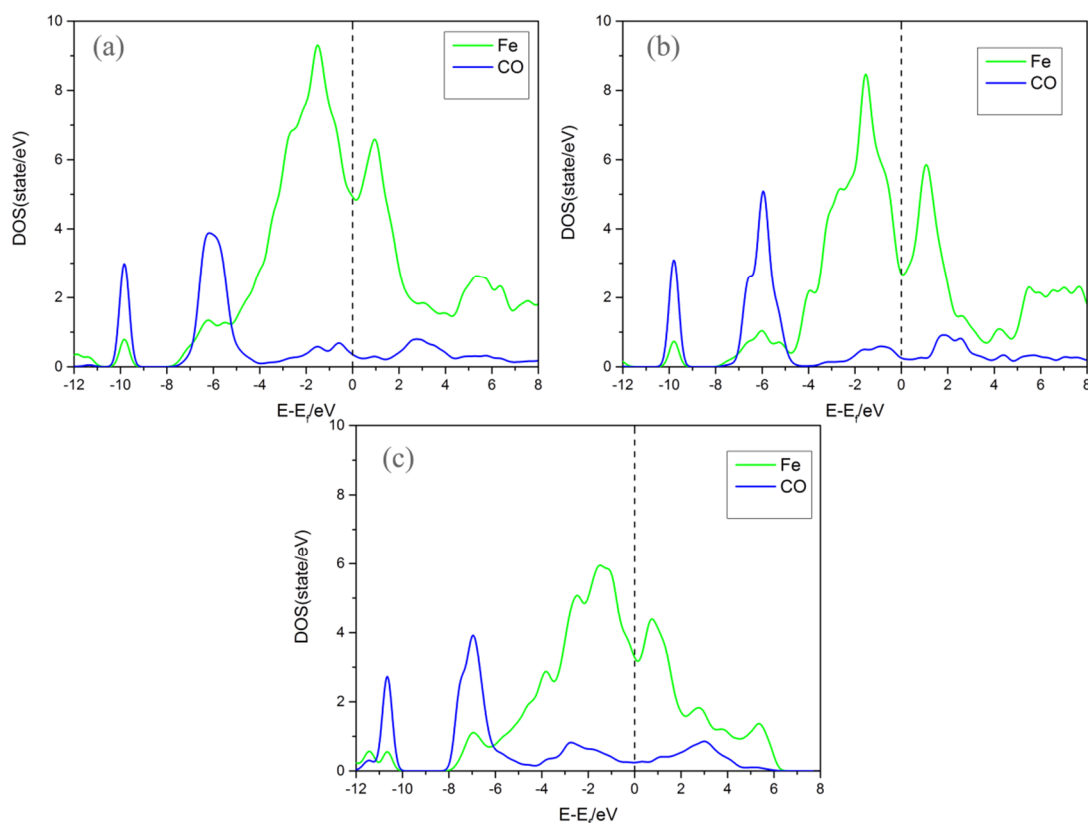
Figure 5. LDOS of CO and its corresponding Fe atom (**a**. $\left(1\overline{11}\right)$4F3; **b**. (001)3F1; **c**. $\left(1\overline{1}1\right)$3F2).

4. Conclusions

In this study, the crystal structure characteristics of h-Fe_7C_3, as well as the adsorption and activation of CO on its low Miller index crystal planes, were studied through the first-principles method of density functional theory. The results show that the low Miller index crystal plane of the h-Fe_7C_3 crystal has multiple equivalent crystal planes; in fact, the maximum adsorption energy of CO on the $\left(1\overline{1}1\right)$ plane is −2.50 eV, indicating that h-Fe_7C_3 has better CO adsorption performance. In addition, the defects generated by the cut-off position of the h-Fe_7C_3 crystal plane have a greater effect on the adsorption energy of CO on its surface, that is, the adsorption energy of CO on Fe atoms with C vacancies is higher. The activity after CO adsorption is greatly affected by the adsorption configuration and is less affected by the adsorption energy. The higher the coordination number of Fe atoms after adsorption, the higher the CO activity. In addition, the bonding of O and Fe atoms is beneficial to the activation of CO.

Author Contributions: Writing—original draft preparation, J.F.; writing—review and editing, D.S., Z.C., J.Z. and H.D. All authors have read and agreed to the published version of the manuscript.

Conflicts of Interest: The authors declare no conflict of interest. The funders had no role in the design of the study.

References

1. Fischer, F.; Tropsch, H. The preparation of synthetic oil mixtures (synthol) from carbon monoxide and hydrogen. *Brennst. Chem.* **1923**, *4*, 276–285.
2. Fischer, F.; Tropsch, H. The synthesis of petroleum at atmospheric pressures from gasification products of coal. *Brennst. Chem.* **1926**, *7*, 97–104.
3. Huang, G.; Li, X.; Yang, Y.; Zhang, B.; Jin, Y.; Shi, X. Development status direction of coal to oil technology in China. *Petrochem. Technol. Appl.* **2017**, *35*, 421–428.

4.	Zhang, Q.; Kang, J.; Wang, Y. Development of Novel Catalysts for Fischer-Tropsch Synthesis: Tuning the Product Selectivity. *ChemCatChem* **2010**, *2*, 1030–1058. [CrossRef]

5.	Wu, P.; Chou, W.; Wang, P.; Luo, M. Effect of precipitation temperature on the catalytic properties of precipitated iron in Fischer-Tropsch synthesis. *Petrochem. Technol.* **2019**, *48*, 243–248.

6.	Wang, X.; Meng, Z.; Lyu, Y.; Li, Y. Research advances in reduction mechanism and kinetics of iron—Based Fisher—Tropsch catalyst. *Clean Coal Technol.* **2017**, *23*, 1–7.

7.	Shroff, M.; Kalakkad, D.; Coulter, K.; Kohler, S.; Harrington, M.; Jackson, N.; Sault, A.; Datye, A.K. Activation of Precipitated Iron Fischer-Tropsch Synthesis Catalysts. *J. Catal.* **1995**, *156*, 185–207. [CrossRef]

8.	Yang, X.; Zhang, H.; Huo, C.; Liu, H. Effects of phase and structure of $Fe_{1-x}O$-based fused iron catalyst on its performance for producing light olefins from syngas. *Petrochem. Technol.* **2018**, *47*, 775–780.

9.	Rao, K.R.P.M.; Huggins, F.E.; Mahajan, V.; Huffman, G.P.; Bukur, D.B.; Rao, V.U.S. Mössbauer study of CO-precipitated Fischer-Tropsch iron catalysts. *Hyperfine Interact.* **1994**, *93*, 1751–1754. [CrossRef]

10.	Chang, Q.; Zhang, C.; Liu, C.; Wei, Y.; Cheruvathur, A.V.; Dugulan, A.I.; Niemantsverdriet, J.W.; Liu, X.; He, Y.; Qing, M.; et al. Relationship between Iron Carbide Phases (ε-Fe_2C, Fe_7C_3, and χ-Fe_5C_2) and Catalytic Performances of Fe/SiO_2 Fischer–Tropsch Catalysts. *Acs Catal.* **2018**, *8*, 3304–3316. [CrossRef]

11.	Perdew, J.P.; Burke, K.; Ernzerhof, M. Generalized Gradient Approximation Made Simple. *Phys. Rev. Lett.* **1996**, *77*, 3865–3868. [CrossRef] [PubMed]

12.	Perdew, J.P.; Wang, Y. Accurate and simple analytic representation of the electron-gas correlation energy. *Phys. Rev. B* **1992**, *45*, 13244–13249. [CrossRef] [PubMed]

13.	Duan, Y.; Liu, Y.; Chen, Z.; Liu, D.; Yu, E.; Zhang, X.; Fu, H.; Fu, J.; Zhang, J.; Du, H. Amorphous molybdenum sulfide nanocatalysts simultaneously realizing efficient upgrading of residue and synergistic synthesis of 2D MoS_2 nanosheets/carbon hierarchical structures. *Green Chem.* **2020**, *22*, 44–53. [CrossRef]

14.	Ghosh, P.S.; Ali, K.; Vineet, A.; Voleti, A.; Arya, A. Study of structural, mechanical and thermal properties of θ-Fe_3C, o-Fe_7C_3 and h-Fe_7C_3 phases using molecular dynamics simulations. *J. Alloy. Compd.* **2017**, *726*, 989–1002. [CrossRef]

15.	Broos, R.J.P.; Zijlstra, B.; Filot, I.A.W.; Hensen, E.J.M. Quantum-Chemical DFT Study of Direct and H- and C-Assisted CO Dissociation on the χ-Fe_5C_2 Hägg Carbide. *J. Phys. Chem. C* **2018**, *122*, 9929–9938. [CrossRef]

16.	Kowalski, M. Polytypic structures of $(Cr, Fe)_7C_3$ carbides. *J. Appl. Crystallogr.* **1985**, *18*, 430–435. [CrossRef]